metals

MDPI

Article

Ball Burnishing of Friction Stir Welded Aluminum Alloy 2024-T3: Experimental and Numerical Studies

Cyrus Amini [1,*], Ramón Jerez-Mesa [2], Jose Antonio Travieso-Rodriguez [2], Hojjat Mousavi [1], Jordi Lluma-Fuentes [3], Mohammad Damous Zandi [2] and Soran Hassanifard [1]

1 Mechanical Engineering Department, University of Tabriz, 29 Bahman Blvd, Tabriz 5166616471, Iran
2 Mechanical Engineering Department, Escola d'Enginyeria de Barcelona Est, Universitat Politècnica de Catalunya, Carrer d'Eduard Maristany, 10-12, 08019 Barcelona, Spain
3 Material Science and Metallurgical Engineering Department, Universitat Politècnica de Catalunya, Av. Eduard Maristany, 10-14, 08019 Barcelona, Spain
* Correspondence: camini@tabrizu.ac.ir; Tel.: +98-9186178835

Abstract: This paper deals with the improvement of the material surface state of friction stir welding paths modified in situ by plastic deformation through ball burnishing. The metallurgical and topological states of materials joined by this welding technique are typically detrimental to the ulterior performance of the workpiece, and it is believed that ball burnishing can improve these states to enhance functioning. This study is divided into two phases. The first one is experimental and consists of welding aluminum AA2024-T3 plates while combining different tool rotations and welding speeds. Then, the welding line is deformed locally by ball burnishing. The improvement of the topology and deep hardness distribution is measured and discussed, and the evolution of mechanical properties is assessed through tensile tests. The second phase is oriented towards estimating the residual stresses by combining two pre-existing models of friction stir welding and burnishing developed by the same authors using ANSYS®. Friction stir welding experimentation and measurements show a decrease in the values of all measured mechanical properties compared to the original material. The dominant factor affecting the properties and texture of the materials is the rotational speed of the tool, with the rupture point in the tensile test located in the distinct zone with the lowest value of microhardness on the advancing side. The higher the ratio of the rotational speed to the welding speed, the lower the roughness value. Finally, ball burnishing is proven to be an effective method to enhance the surface integrity of friction stir welded joints in light of the results, achieving a reduction of 11% to 36% in average roughness and an increase of about 22% in hardness profile, along with an integrated numerical model estimation of a remarkable effect on compressive residual stresses in-depth on the retreating side of the welded samples. However, in some tests, this treatment reduced some characteristics (yield stress and failure strain).

Keywords: ball burnishing; friction stir welding; integrated numerical model

Citation: Amini, C.; Jerez-Mesa, R.; Travieso-Rodriguez, J.A.; Mousavi, H.; Lluma-Fuentes, J.; Zandi, M.D.; Hassanifard, S. Ball Burnishing of Friction Stir Welded Aluminum Alloy 2024-T3: Experimental and Numerical Studies. *Metals* **2022**, *12*, 1422. https://doi.org/10.3390/met12091422

Academic Editor: Xiangdong Gao

Received: 26 July 2022
Accepted: 24 August 2022
Published: 28 August 2022

1. Introduction

Nearly three decades after its invention, friction stir welding (FSW) is still recognized as a significant solid-state welding technique. The need to obtain defect-free joining of aluminum alloys (i.e., avoiding hot cracking or stress cracking corrosion) has led to a widespread use of FSW as a valid welding method [1,2]. Besides, demand for light and resistant products, high-strength joints, short manufacturing times and lower manufacturing costs have made FSW an increasingly applied process.

The emergence of tensile residual stresses after FSW, regardless of their relatively low value compared to other conventional joining methods, can cause serious problems such as reduced fatigue strength [3]. Moreover, other mechanical properties, such as hardness and tensile strength, are also affected negatively in the thermally affected zone [4].

Many researchers have presented some methods of surface enhancement to improve the mechanical and surface properties after production [5–8], machining [9] or welding processes. All methods currently available result in a layer of compressive residual stresses following tensile deformation. The methods differ primarily in how the surface is deformed and to what magnitude, and in the form of the resulting residual stresses and cold work. Low plasticity burnishing (LPB) or ballburnishing (BB), which is known for providing minimum relaxation and cold work in comparison to other techniques for surface improvement, is a good alternative to be applied to the welding area [10]. Prevey et al. [11] specifically addressed the fatigue improvement of aluminum alloy FSW samples that were subsequently ball burnished. They stated that BB post weld processing left the surface of the FSW specimen on the order of −450 MPa in compression in all directions. In the experimental work, Başak et al. [12] investigated the effect of burnishing on FSW of aluminum alloy. They declared that the number of passes is one of the most relevant burnishing parameters affecting the surface roughness. They also claimed that under the optimal parameter set, although hardness and roughness improve, the burnishing process may negatively affect the material's strength. Huang et al. [13], by developing a new technique of in situ rolling FSW in which the burnishing and welding tools are used simultaneously, reduced the residual stress and distortion. Rodriguez et al. [14] investigated and described the effect of BB of FSW aluminum alloy on the mechanical properties such as roughness and hardness. They stated that the most determinant factor in the increase of surface hardness is the burnishing force.

Based on the above findings, BB can be considered as one of the methods to improve the welding surface, as it causes an increase in the residual hardness, while the roughness decreases and the tensile residual stress on the surface becomes compressive. Nevertheless, no studies have reported a comprehensive numerical model to investigate the distribution of residual stress due to BB on FSW samples. For this reason, the main novelty of this paper is to present an integrated 3D-numerical model between FSW and BB. To this end, the authors of this paper have already developed a numerical model to simulate friction stir welding, the validity of which has been confirmed by experimental measurements [15]. Residual plastic stresses and strain tensors after cooling and release of fixtures, as well as the plastic behavior of the weld area obtained from the uniaxial tensile test, were applied as the initial input conditions in this study. Then, by performing the burnishing process on, residual stress distributions along the surface and through the thickness in the design of the experiment were obtained. The feasibility of this integrated model is validated by comparing the predicted results with other articles.

This paper also experimentally focuses on hardness distribution, surface roughness and tensile strength for FSW samples with BB and without it. The effect of FSW parameters (rotational and welding speed) on the mentioned mechanical properties has been investigated. These examinations are limited to the welded affected area. Comparisons show that the burnishing process can enhance and improve the effect on the measured mechanical properties.

2. Materials and Methods

2.1. Experimentation

The plates selected as the targets to be treated through FSW and BB were made of AA2024-T3 aluminum alloy of 3 mm thickness, 80 mm width and 100 mm length. The chemical composition of the workpiece (as specified by the supplier ALCOA Inc., Pitssburg, PA, USA) has been detailed in Table 1. A FSW tool with a tapered pin was used to join the plates. The height of the pin was 2.7 mm and the pin diameter at the top and the tip were 5.5 mm and 4.5 mm, respectively. The diameter of the shoulder was 14 mm (shown in Figure 1a). The tool was made up of tungsten carbide. The experimental outline is shown in Figure 1b [15]. The burnishing tool applied hereafter is based on the design patented in Spain and France with number ES2615002 [16]. The prototype is based on spring compression to control the burnishing preload. The diameter of the ball in the

burnishing tool was 10 mm (see Figure 2a). The burnishing process with advancing speed of 1000 mm/min (in the burnishing direction) was performed on an area with a width of 16 mm and a length of 35 mm in the middle of the weld line (Figure 2b).

Table 1. Standard chemical composition of AA2024-T3 alloy.

Element	Si	Fe	Cu	Mn	Mg	Cr	Zn	Ti	Al
Weight%	0.13	0.5	4.8	0.72	1.41	0.1	0.07	0.15	Balanced

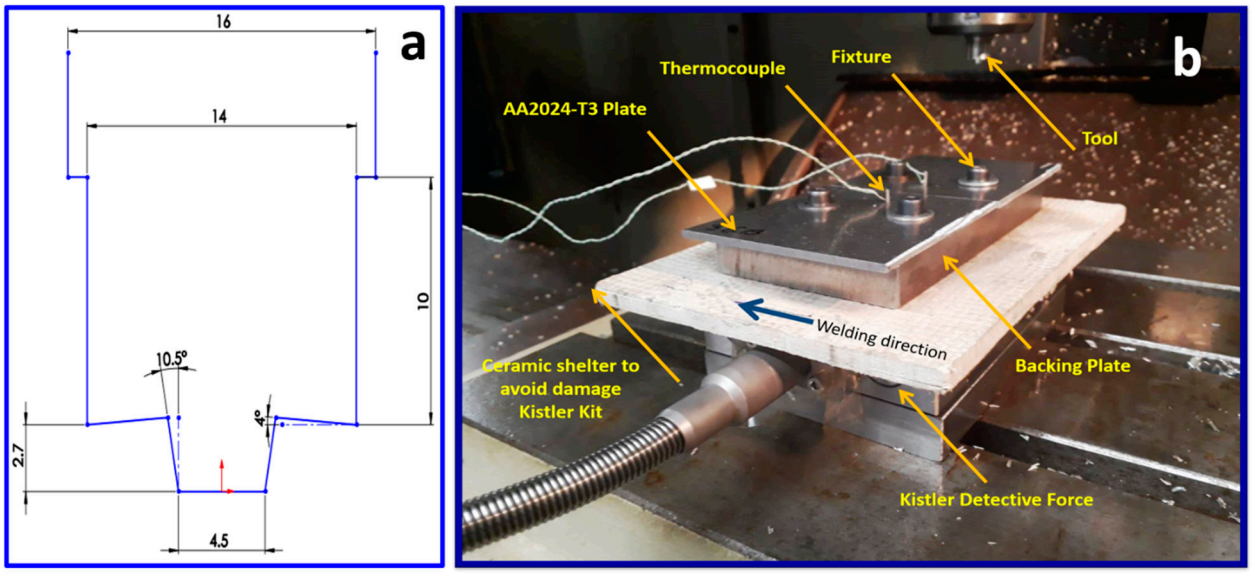

Figure 1. (**a**) Dimensions of FSW tool (mm); (**b**) set up for FSW process (reproduced and adopted from [15] with permission from Springer, 2022).

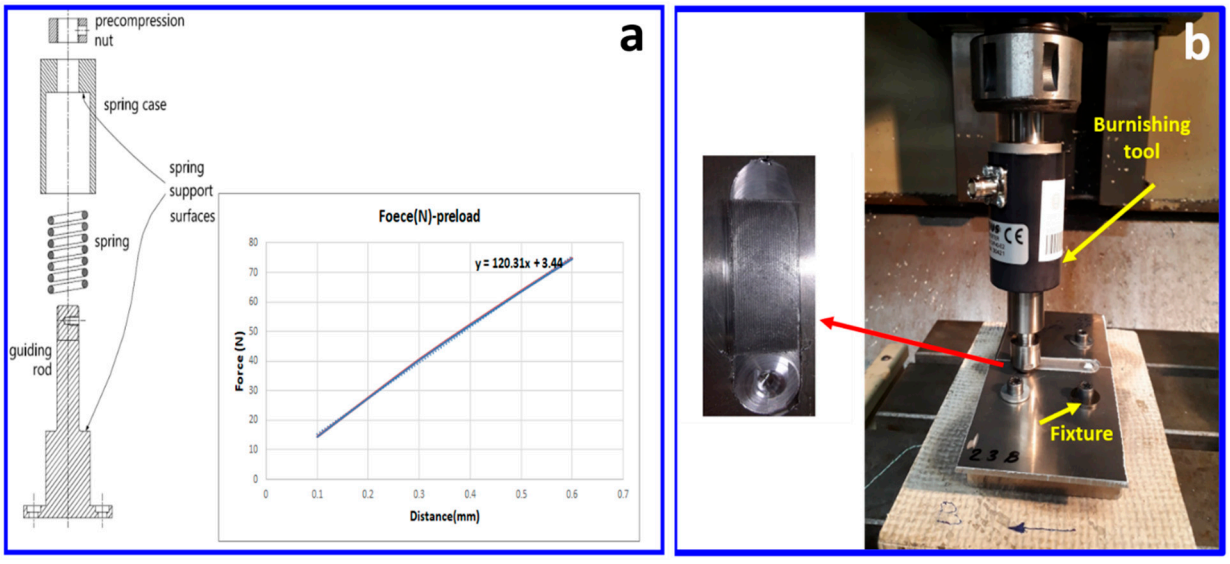

Figure 2. (**a**) Exploded view of BB tool [16]; (**b**) set up for BB process.

A calibration process was executed to find that a burnishing force of 170 N was adequate to treat the specimens. The welded plates were mounted on a dynamometric table of forces Kistler type 9129AA (Kistler Group, Winterthur, Switzerland) that allowed the registration of both the vertical burnishing load and the radial forces experienced by the burnishing tool as it advanced on the workpiece (shown in Figure 3).

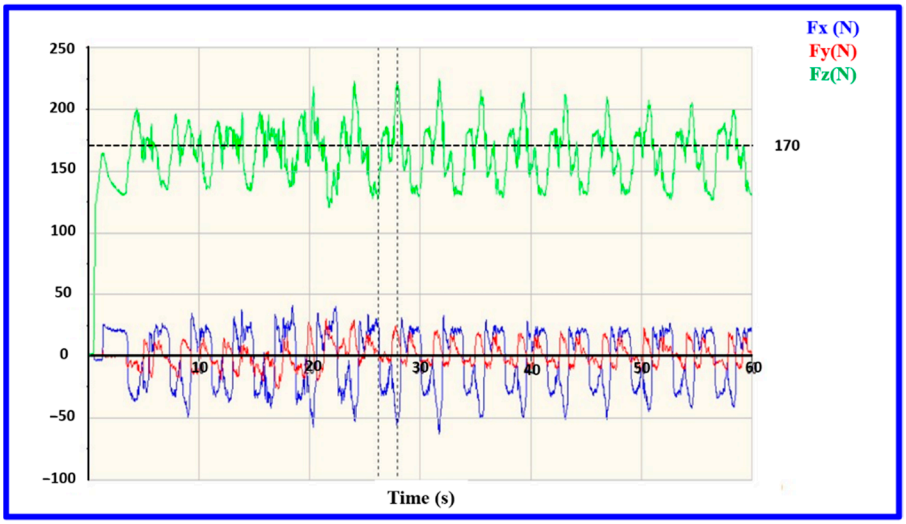

Figure 3. Vertical load (F_z) and radial friction force (Fx and Fy) during BB.

An experimental design of two factors with two levels and one central point was used to run the FSW tests (summarized in Table 2). Both the BB and FSW process were conducted in a milling machine MC 600 (LAGUN, Azkoitia, Spain) with maximum power of 5 kW. Furthermore, during the FSW process, plunge depth and tool penetration rate were 2.95 mm and 3 mm/min, respectively. The tilt angle used in this study was zero (due to the limitation of degree of freedom in the milling machine).

Table 2. Design of experiments for aluminum alloy AA2024-T3 workpieces.

Test	FSW Parameters		BB Parameters	
No.	Rotational Speed (rpm)	Welding Speed (mm/min)	Lateral Feed for Burnishing (mm)	Burnishing Force (N)
1	550	20	0.3	170
2	550	40		
3	825	30		
4	1100	20		
5	1100	40		

In order to allow high-resolution 3D microtopography and the analysis of shapes and textures, a Micromesure 2 (STIL MARPOSS, Saint Hilaire, France) was used. A scope with -2.5 mm $< x <$ 2.5 mm and -2.5 mm $< y <$ 2.5 mm in the middle of the welding area was considered. Here, the Z axis is out of plane. The scanning velocity was set to 5 mm/s. All parameters for the texture, according to ISO 4287 standards, were approximated with a 0.1 nm resolution. Then, a microhardness tester Micromet 5114 (BUEHLER, Lake Bluff, IL, USA) was used to estimate hardness. The material hardness was measured through a Vickers micro-indentation test, applying 500 gr load on the burnished area in the welded area at the specimen's surface.

Finally, to introduce the stress–strain curve, in a universal test machine EM2/20 series (Microtest, Madrid, Spain), uniaxial tensile tests using an extensometer (to record the deformation) were performed. The tests and specimens were designed and performed according to the ASTM E646-00 standard (shown in Figure 4), with a strain rate of 1.2 mm/min.

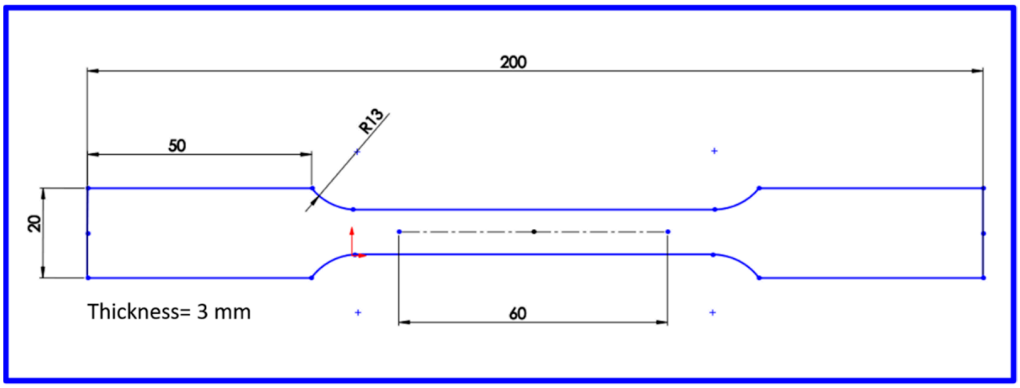

Figure 4. Dimensions of the tensile specimens according to ASTM E64-00 standard (mm).

2.2. 3D Finite Element Simulation

To simulate the three-dimensional FSW and BB process, commercial FEM (Finite Element Method) software ANSYS (version 17.02, Ansys Inc., Canonsburg, Pennsylvania, PA, USA) was used. The full formulations about heat generation, boundary conditions and contact mechanism (using modified Coulomb criteria) are described in Amini et al. [15]. It has already been shown that temperature-dependent multilinear isotropic hardening using the compressive stress–strain data at a strain rate of 10 s^{-1} can deliver a good approximation of rate-dependent plastic behavior in the aluminum alloy FSW process [15]. Based on a Lagrangian approach, a 3D 20-node SOLID 226 element with coupled-field (structural-thermal) capabilities was used to simulate FSW. To this end, a hexahedral mesh to avoid mesh-orientation dependency with dropped midside nodes was selected, because quadratic shape functions lead to oscillations in thermal solutions, resulting in nonphysical temperature distribution.

The simulation process exploits experimental arrangement of FSW and is implemented in five steps using transient analysis as follows: plunge, dwell, linear welding, retraction, cooling and fixture release. At the end of this process, by creating special macro-(residual) plastic stress and strain tensors (regardless of temperature as a DOF (degree of freedom)) are extracted for each element and are preserved as the initial state file to be recalled in the next process.

In the BB simulation, the ball tool is considered rigid and applied in a zigzag tool path. The cycle of the load imposed on the ball can be controlled by the displacement control method [17]. A vertical displacement corresponding to the phase of penetration into the material (due to the axial load of 170 N) is applied as the load. Then, the ball moves (along the +Y-axis) and rotates freely (about its center). Lateral feed occurs by moving the ball (along the −X-axis) and rotating (about its center). The first cycle of loading is completed when the ball moves (along the −Y-axis) and rotates freely. These cycles are repeated to cover the weld zone. During the BB process, the top surface of the plates is fixed at four zones. A fixed zone can be represented as a bolt and nut fixed to the clamp. The boundary condition used for the FEM is represented by imposing that the displacement of these nodes is zero (U = 0) (depicted in Figure 5). On the other hand, the bottom surface of the raw material supported by the backing plate is assumed to be fixed in the normal direction: $U_z = 0$.

Plate dimensions and meshing are the same as in the FSW simulation. Owing to the small effect of inertia, static analysis was performed. On the other hand, due to the fact that the analysis is independent of temperature, the element type was changed to SOLID 185. From a structural point of view, this element type is compatible with SOLID 226 (with dropped midside nodes). SOLID 185 is defined by eight nodes with three degrees of freedom at each node: translations in the nodal X, Y and Z directions (shown in Figure 5). Contact element types CONTA174 and TARGE170 were used to model the surface-to-surface contact between the ball and plates. The augmented Lagrange method was chosen as the contact algorithm. Similar to the meshing process in Reference [15] for

FSW simulation, for each plate, the number of divisions (NDV) is 30 with an aspect ratio (ASR) of 0.1 along the X-axis. The NDV is 44 and the ASR is 1 along the Y-axis. Along the thickness (Z-axis), the NDV is 3 and the ASR is 1. To make FEM models of plates, the number of elements and nodes are 5280 and 12,712, respectively.

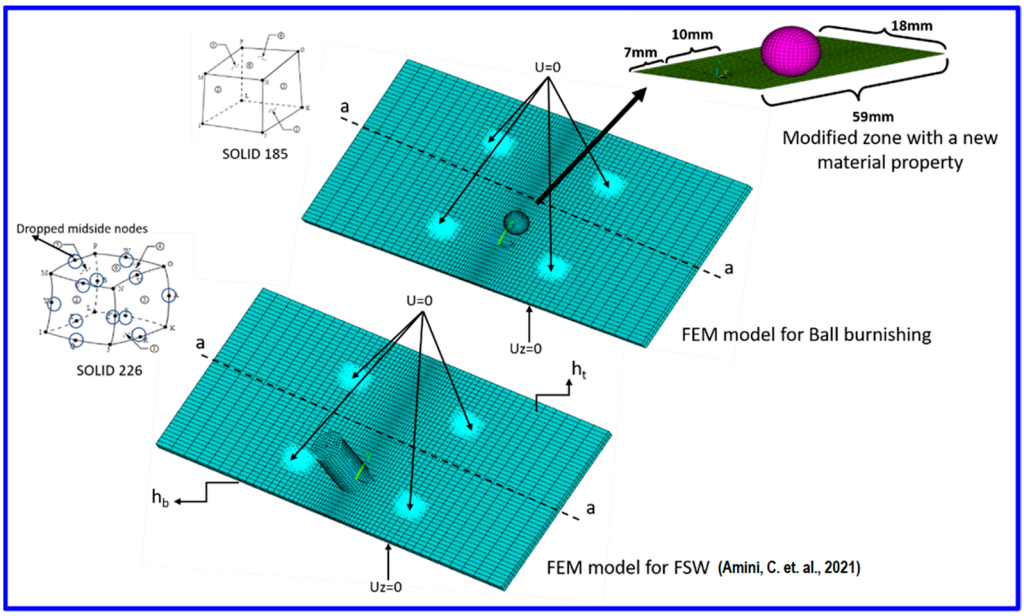

Figure 5. Display of FEM model for integrated numerical model between FSW and BB, adapted with permission from Ref. [15]. 2021, Springer Nature BV.

The contact behavior at the interface between two plates is changed from bonding (in the FSW simulation) to always bonding (in the BB simulation). Microstructural examination of the FSW joints revealed the presence of some distinct zones such as the thermomechanical heat-affected zone (TMAZ) and the heat-affected zone (HAZ). After welding, the structural properties of the materials that are in contact or in close proximity to the weld line change. To estimate plastic behavior in this area (welding zone), uniaxial tensile tests were conducted on FSW samples. The strain–stress curve was assigned to this area as an estimation of average behavior of the welding zone. To this end, multilinear isotropic hardening is presented as the plasticity model because:

1. Attempts are made to maintain the integrity of the model by considering the same hardening model used in FSW simulation;
2. The effectiveness of isotropic hardening model to simulate BB has already been proven and cited by other authors [18–20];
3. Combined isotropic and kinematic hardening has been reported in BB simulation [21]. However, due to the unavailability of Chaboche kinematic hardening for the FSW zone of aluminum alloy 2024-T3, isotropic hardening was a suitable candidate for a hardening model.

Using a hardness test, the width of the area is roughly distinguished from the border of the parent material. Here, 9 mm away from center line (along the transverse) is considered as the border of the material in the welding zone (depicted in Figure 5).

Gaussian points were defined to detect the contact areas between the ball and the surface, governed by Coulomb–Mohr's frictional model without cohesion as follows [22]:

$$\tau = \mu p_b \quad (1)$$

where τ is the frictional shear stress at the contact surface and μ is the coefficient of friction, which is assumed to be 0.15 and constant during the simulation with respect to [22]. p_b is the burnishing pressure due to the contact of the ball and the surface material, which

is obtained by dividing burnishing force (F_b) to contact area (A_b) between the ball and the material.

Generally speaking, every simulation included in Table 2, from FSW to BB for every test, was composed of a sequence of loading steps represented by the flowchart in Figure 6.

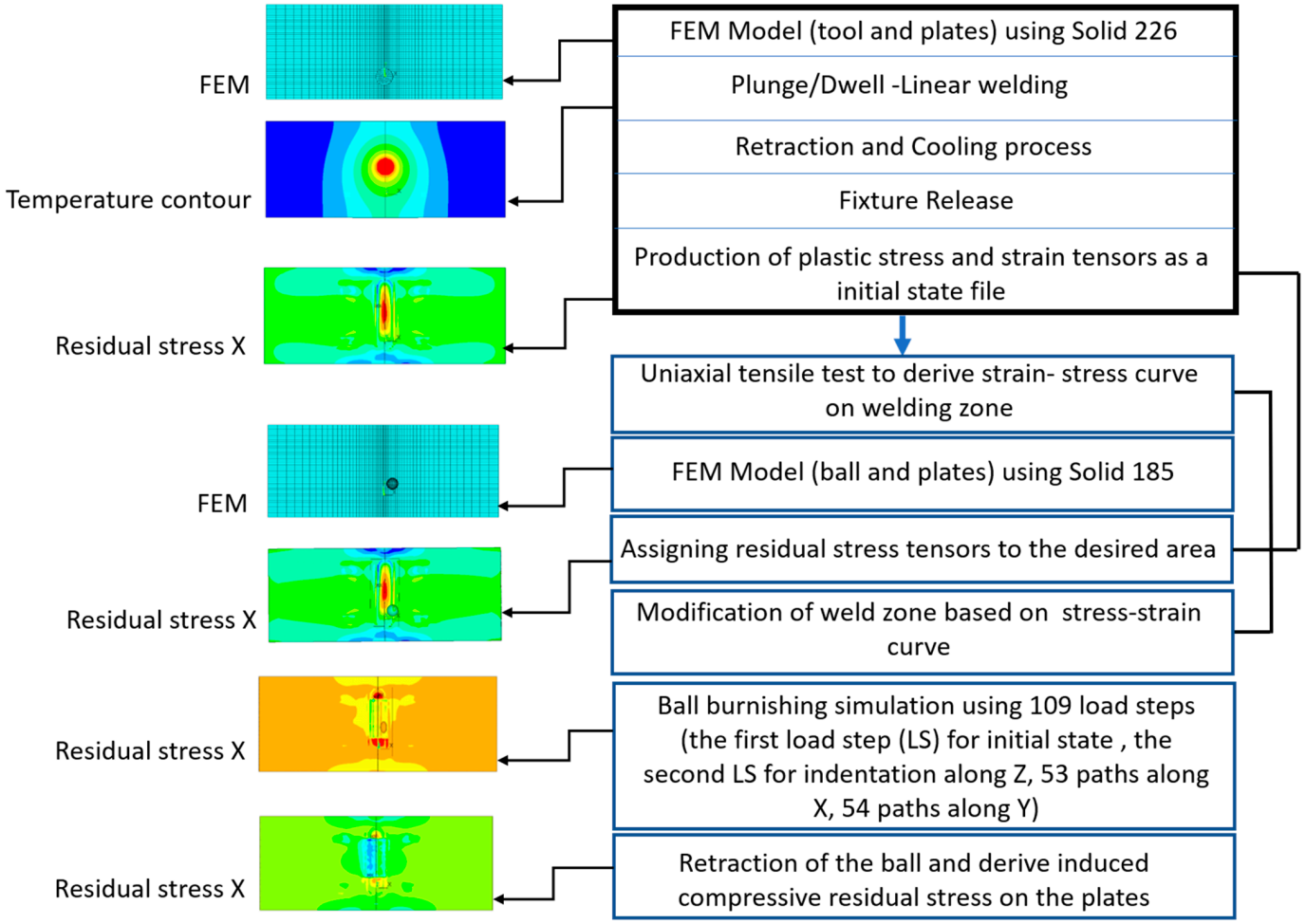

Figure 6. Flowchart representing the simulation steps from FSW to BB process.

3. Results and Discussion

The results presented in this section are divided into four sub-sections: surface texture, material hardness at the surface, tensile mechanical properties and numerical simulation for estimating residual stress in an integrated numerical model.

3.1. Surface Texture

In this part of the study, the effect of FSW parameters and the burnishing process (applied with constant parameters in the welding zone of AA2024-T3) on the surface texture are investigated. Figure 7 shows that increasing rotational speed enhances surface texture (35% decrease in average roughness), so that S_a and S_q of 3.76 and 4.61 µm at lower rotational speed (ω = 550 rpm) decrease to 2.41 and 3.69 µm at higher rotational speed (ω = 1100 rpm), respectively, while rising welding speed results in higher values of S_a and S_q (an increase of 1.5 to 3.3% in roughness average). This is in agreement with Reference [23]. The best quality occurs in Test 3 (ω = 825 rpm). It seems that the higher the ratio of rotational speed to welding speed, the lower the roughness.

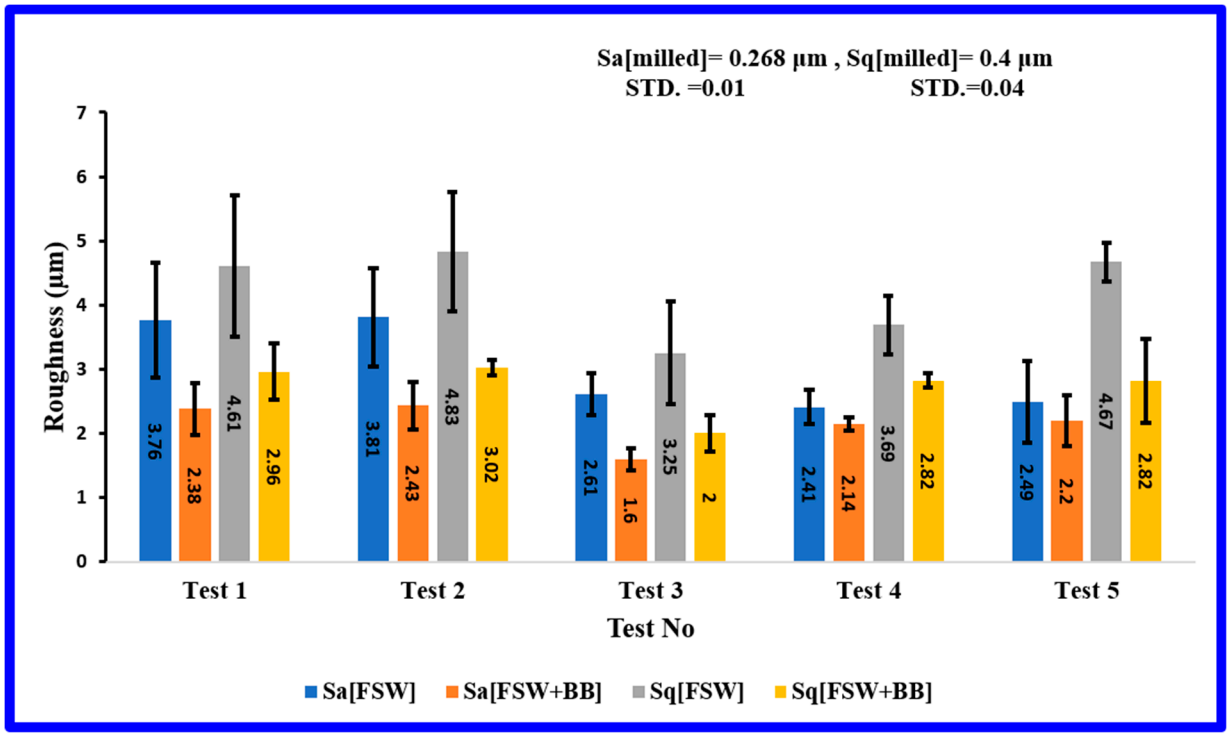

Figure 7. Surface amplitude descriptive parameters with their standard deviation (STD) for the surface (before FSW, after FSW and after BB).

Plastic deformation created by BB affects peaks and valleys. It improves the formation and appearance of a new surface texture. Here, regardless of the parameter with which the welding is performed, the effectiveness of BB on the surface roughness after FSW is noticeable (see Figure 8).

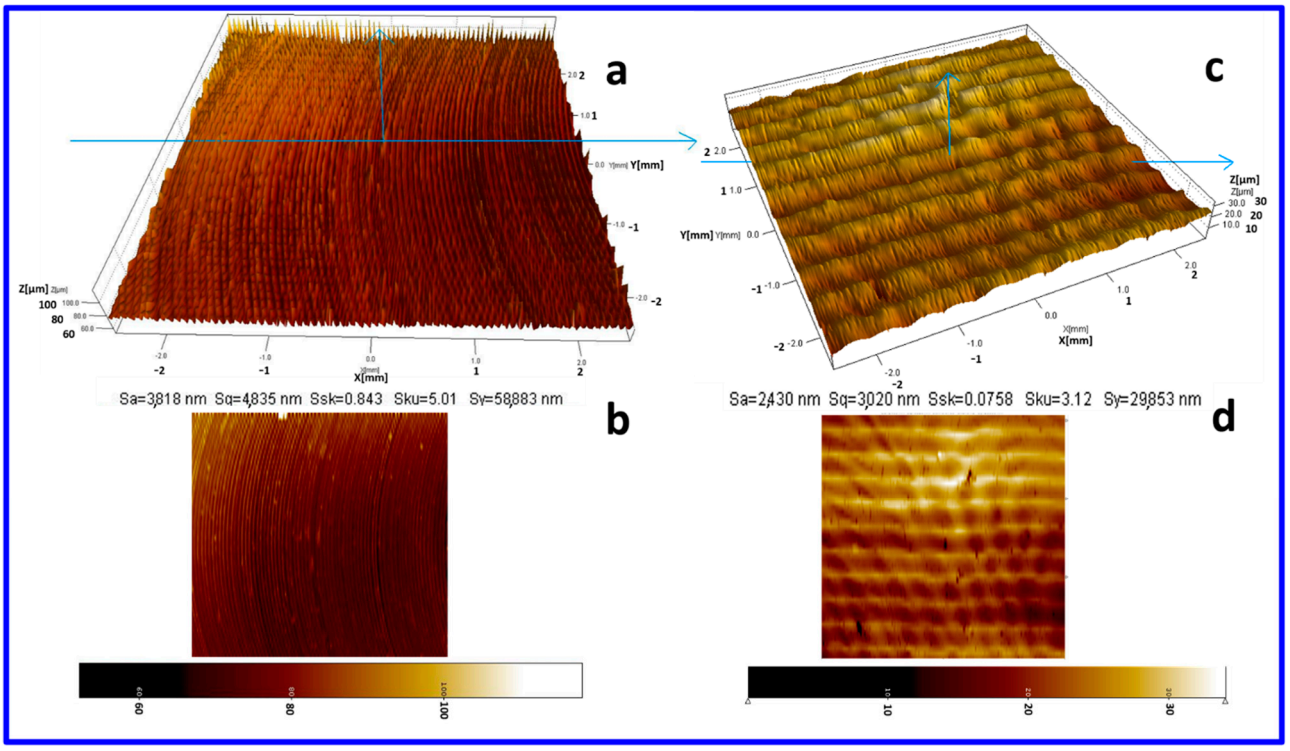

Figure 8. Surface topography and texture for Test 2: (**a**) surface 3D topography; (**b**) image report of roughness after FSW; (**c**) surface 3D topography; (**d**) image report of roughness after BB.

The effect of BB on surface quality improvement is more pronounced in specimens where welding was performed at low rotational speeds, as the reduction in average roughness (S_a) was 36% in tests 1 and 2, while it is 11% in tests 4 and 5. IN all tests after BB, S_q experienced reductions of 23 to 39% compared to FSW samples. Although the surface texture is improved by applying the burnishing process to the welded specimens, the quality of surface roughness is still lower than the initial surface of the specimens before welding (see Figure 7).

3.2. Hardness Distribution

Some researchers have shown that the greatest improvement in the hardness of welded specimens is achieved when the burnishing operation is performed parallel to the welding direction [14]. For this reason, in the present paper, BB was performed in the direction of welding and microhardness was measured along the transverse path passing through the middle of the weld line. Figure 9 shows the microhardness evolution through the welding zone of FSW aluminum alloy samples before and after burnishing. The obtained profiles show asymmetry with respect to the centerline along the weld. In all measured post-welding hardness profiles, the welding area has a lower hardness than the parent material.

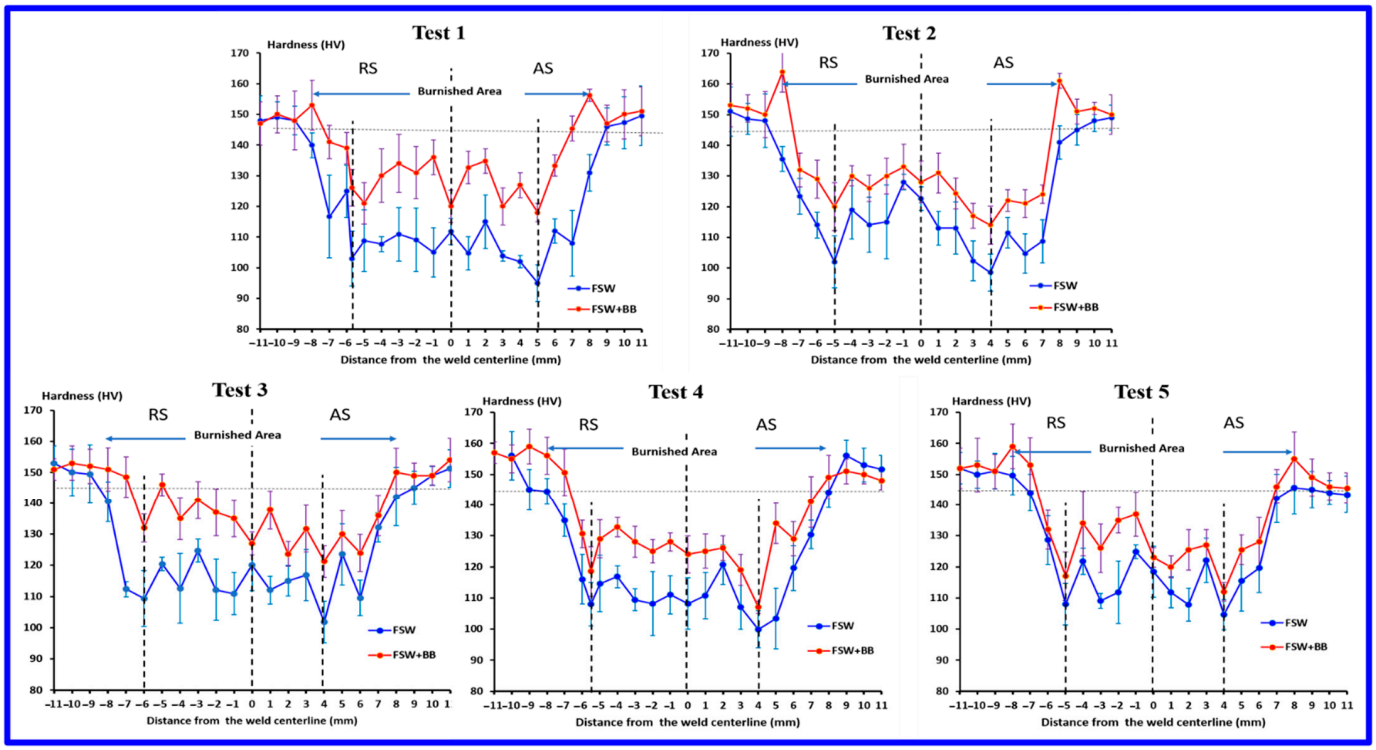

Figure 9. Comparison of microhardness evolution with/without burnishing at the surface in the welding zone along the transverse path (passing through the middle of the weld line).

The value of the hardness profile (blue graphs) on the retreating side (RS) is somewhat higher than on the advancing side (AS). Another significant point of this story is that the simulations showed that areas that experience a higher temperature cycle [15] usually show less hardness in experimental measurements. The maximum temperature range occurs between 4 to 5 mm from the center of the weld line in the AS region and the same range in the hardness profile has the lowest values, as was also concluded in [23].

In a way, it can be concluded that welding in this range is also more vulnerable to rupture, because the simple tensile tests of the FSWed and FSW + ball burnished specimens in this study all ruptured at some point in the AS region (see Section 3.3). The hardness profile in the AS and the RS each have a minimum point, and the minimum observed in the AS area is less than that in the RS area. These minimum points seem to indicate the

approximate position of the transition from TMAZ to HAZ in the weld structure, at which point, severe joint softening is created by the coarsening of grains [24]. Interestingly, the minimum point distance in the AS from the center of the weld is less than its corresponding point in the RS. Comparing Test 1 to Test 2 and Test 4 to Test 5 (hardness profile of welding), it seems that increasing the welding speed reduces the softening degree and improves the hardness in the nugget zone because of the short exposure time at high temperature, which is in line with [24,25].

The effect of burnishing improvement is more noticeable in places where the hardness has been greatly reduced after welding and that are somewhat softer (areas in the proximity of NZ). The greatest improvement in the minimum points of the hardness profile, occurring in Test 1, is 23 on Vickers scale. At a distance of 8 mm from the weld line, which is the border of the burnished area, the maximum hardness is observed, which increased from around 15 to 20 HV compared to the hardness of the raw material during all tests. Although the burnishing process resulted in an increase of 37 HV in some welding points (x = ±7 mm in Tests 1 and 3, respectively), on average, this process raised the hardness up to 22% among all tests. Of course, the effectiveness of the treatment can be increased by up to 40% by raising the burnishing force (as long as the welding microstructures are not damaged) [14]. Interestingly, the locations of points with the minimum value in the hardness profile of the weld are still the same as the locations of points with the lowest value of hardness in the hardness profile in the burnished specimens (see Figure 9). In other words, the range of failure points in the tensile test for the welded specimen and the welded specimen under burnishing will remain almost constant and only the amount of fracture force will be different.

3.3. Tensile Mechanical Properties

The purpose of the tensile test is to determine mechanical properties of aluminum alloy samples before and after FSW and after FSW + BB. In the tensile test, Young's modulus (E), tangential modulus (E_T), yield stress (σ_y), ultimate tensile stress (UTS) and failure strain (ε_f) were measured after each process and the corresponding parameters for each of them were compared.

3.3.1. Tensile Test for Aluminum Alloy and Weld Specimens

In order to determine whether the parent material is isotropic or not and obtain the initial stress–strain curve, tensile tests were performed in the roll direction and perpendicular to it. Although the material behavior deviates to some extent from the ideal isotropic (for example, Young's modulus is greater in the direction perpendicular to the rolling), the differences in the two directions perpendicular to each other are not significant, and therefore the overall average of the parameters in the twelve tensile tests is considered as characteristic of the stress–strain curve, which is presented at Table 3; its diagram is shown in Figure 10. Figure 10 a shows the specimens after the tensile test, all of which have ruptured close to the fillet zone of the specimen at the top or bottom. The fracture planes, which are planes of maximum shear stress, make a theoretical angle of 45° with the sample length.

Table 3. Mean characteristics of strain–stress curve in tensile test before FSW.

Item	Young's Modulus (GPa)	Tangential Modulus (GPa)	Yield Stress (MPa)	UTS (MPa)	Failure Strain (%)
Mean	71.8	0.006	344	464.5	11.1
STD.	1.97	0.0023	3.8	8.8	1.2

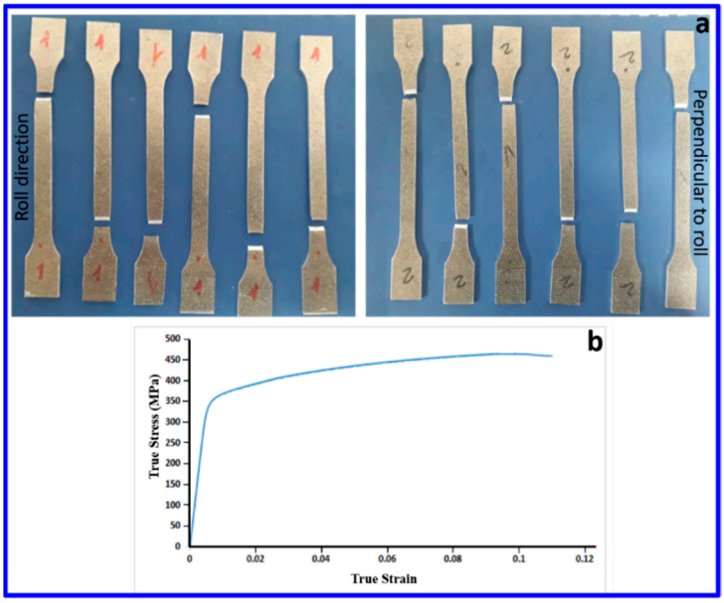

Figure 10. (**a**) Tensile test samples after failure; (**b**) mean stress–strain curve of aluminum alloy 2024-T3.

It is worth noting that not all FSW tests performed in this experiment necessarily resulted in a sound weld, as some common defections appeared in tests 1 and 2.

After performing the FSW process, the specimens were subjected to a tensile test. Most of the studied characteristics in the stress–strain curve were reduced compared to the parent material. Another important point that was common to all specimens is the rupture position. They all fractured in the AS near the pin (between the pin radius and the shoulder radius), which is approximately the boundary of the transition from TMAZ to HAZ. At the advancing side, the material experiences high cycle temperature, which leads to a coarser grain size without dynamic recrystallization occurring, and the sample will break in this region [26]. However, due to low heat input or the lack of sufficient strain rate in welding tests [26] that are performed at a lower rotational speed (tests 1 and 2), some defects such as tunnels and flash at the margin of the weld line will form. Here, the failure line is closer to the center line of the weld and occurs almost at the pin radius (see Figure 11).

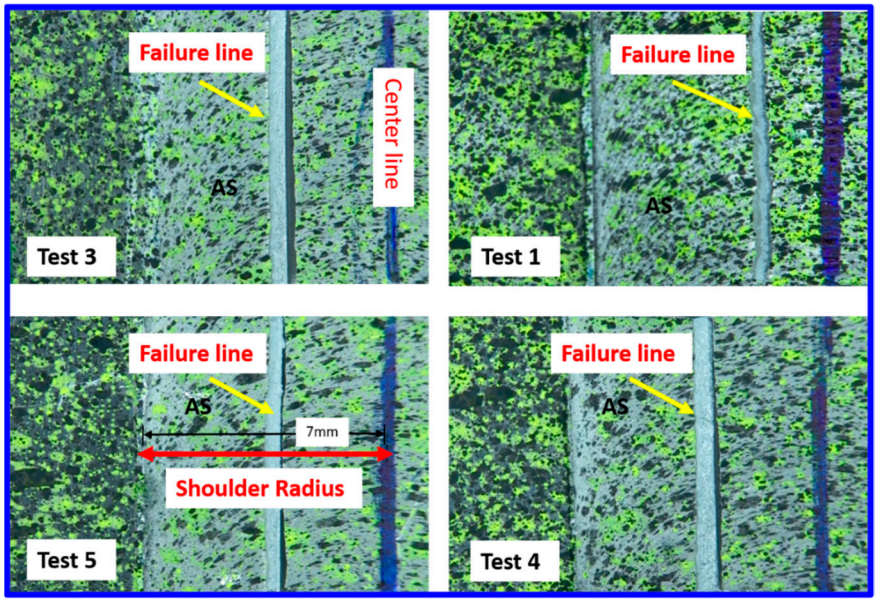

Figure 11. Fracture line location in four FSW tests after the simple tensile test.

Researchers already have tried to exploit precise methods (i.e., nanoindentation or ultrasonics) to measure E in FSW samples by considering the regions in the FSW. They reported that this parameter has a decrease of 1.2% in HAZ and an increase of 4.6% in NZ [27]. Generally speaking, they are unanimous that Young's modulus is a microstructure-independent mechanical property that is dependent on the composition, so the FSW process has almost no significant effect on this characteristic [27,28]. Here, by considering a mean value for E, its variation range compared to the parent material is less than +6% and −2%, and it can be assumed to be unchanged (see Table 3). E_T is defined as the slope of the stress–strain curve, and is mostly used to describe the stiffness of a material in the plastic range. This study showed that, in general, the FSW process causes an increase in E_T. In other words, as the slope of the plastic curve increases, the ductility of the material behavior decreases and tends to become brittle. Here, specimens welded at low rotational speeds have the greatest increase in this characteristic (see the value of E_T for tests 1 and 5 in Table 4).

Table 4. Measured E and E_T for FSW and FSW + BB specimens.

Parent Material		Test	FSW		FSW + BB	
E (MPa)	E_T (MPa)		E (MPa)	E_T (MPa)	E (MPa)	E_T (MPa)
71.8	0.0006	1	67.5	0.133	66	0.016
		2	69.5	0.022	70	0.017
		3	73.9	0.013	76	0.037
		4	71.5	0.02	73	0.02
		5	70.1	0.007	68	0.041

After welding, the σ_y of specimens experienced a decrease of 58 to 63% (ω = 550 rpm) and 36 to 42% ($\omega \geq$ 825 rpm) compared to the parent material. It can be said that welding tests in this experiment that were carried out at rotational speeds higher than 825 rpm, have the highest σ_y before failure, so they sustain 58 to 64% of the σ_y of the main material. The *UTS* of as-welded samples ranges from 27 to 55% of that of the parent material. Similar to the yield stress, high-speed welds ($\omega \geq$ 825 rpm) have the highest value of *UTS*. The maximum value of *UTS* was obtained in Test 3. Failure strain is another characteristic of the stress–strain curve that is affected by the welding process. ε_f of as-welded specimens decreases compared to that of the base material. The maximum and minimum values of failure strain of 3.53% and 0.71% were witnessed in tests 1 and 3, respectively. Figure 12 signifies that compared to tests 1 and 2, tests performed at rotational speeds greater than 825 rpm have higher ε_f. By observing the changes in the characteristics of FSWed samples compared to the parent material, it can be concluded that the dominant factor that affects characteristics of the strain–stress curve is the rotational speed of the tool.

3.3.2. Tensile Test for FSW Samples under BB Process

The execution of BB on FSW samples delivers distinctive effects on mechanical properties. This process enhances some mechanical characteristics after welding and makes some worse. Here, similar to welded samples, the location of the failure line is located in the AS zone at the border of the pin radius or between the pin and shoulder radius.

In the case of E after the burnishing process, because the variation range in this parameter is less than ±3% compared to that of FSW samples, its changes are neglected and it is assumed to be constant. The BB process has a different effect on the E_T of welding tests. It raises E_T for tests conducted at high rotational speed ($\omega \geq$ 825 rpm) and decreases E_T for tests performed at lower rotational speed ($\omega <$ 825 rpm). The BB process seems to have the highest change in E_T in the sample of welds performed at high rotational speeds. Compared to the welding sample, after the burnishing, tests 1 and 2 ($\omega <$ 825 rpm) achieve the largest incremental change in the value of the σ_y. Figure 12 shows that the burnishing process on FSWed samples (with higher rotational speed) leads to less increase of the value of the σ_y (tests 3 and 5), or it may even worsen yield stress (test 4). The σ_y of samples under

FSW + BB is 61 to 70% that of the parent material. Similar to yield stress, the burnishing operation enhances the *UTS* of FSW specimens with low rotational speed (ω = 550 rpm), while it may result in a lower increase or may decrease the value of the *UTS* (tests 3 and 5 or test 4, respectively). From the results, it can be found that the maximum and minimum values of *UTS* are obtained in FSW + BB tests 3 and 2, which are 45% and 72% that of the parent material, respectively. Interestingly, when burnishing operations are performed on two FSW samples produced at the same rotational speed, the FSW test that has a higher welding speed will possess greater values of *UTS* and σ_y (compare FSW + BB tests for Test 1 with Test 2, or Test 4 with Test 5 in Figure 12). Running BB on FSW specimens fabricated at ω = 550 rpm causes them to experience a greater value of ε_f than FSW samples. In contrast, this process has an unfavorable effect on FSW tests 3 and 4. After the burnishing, the maximum value of ε_f of 2.9% was witnessed in Test 3.

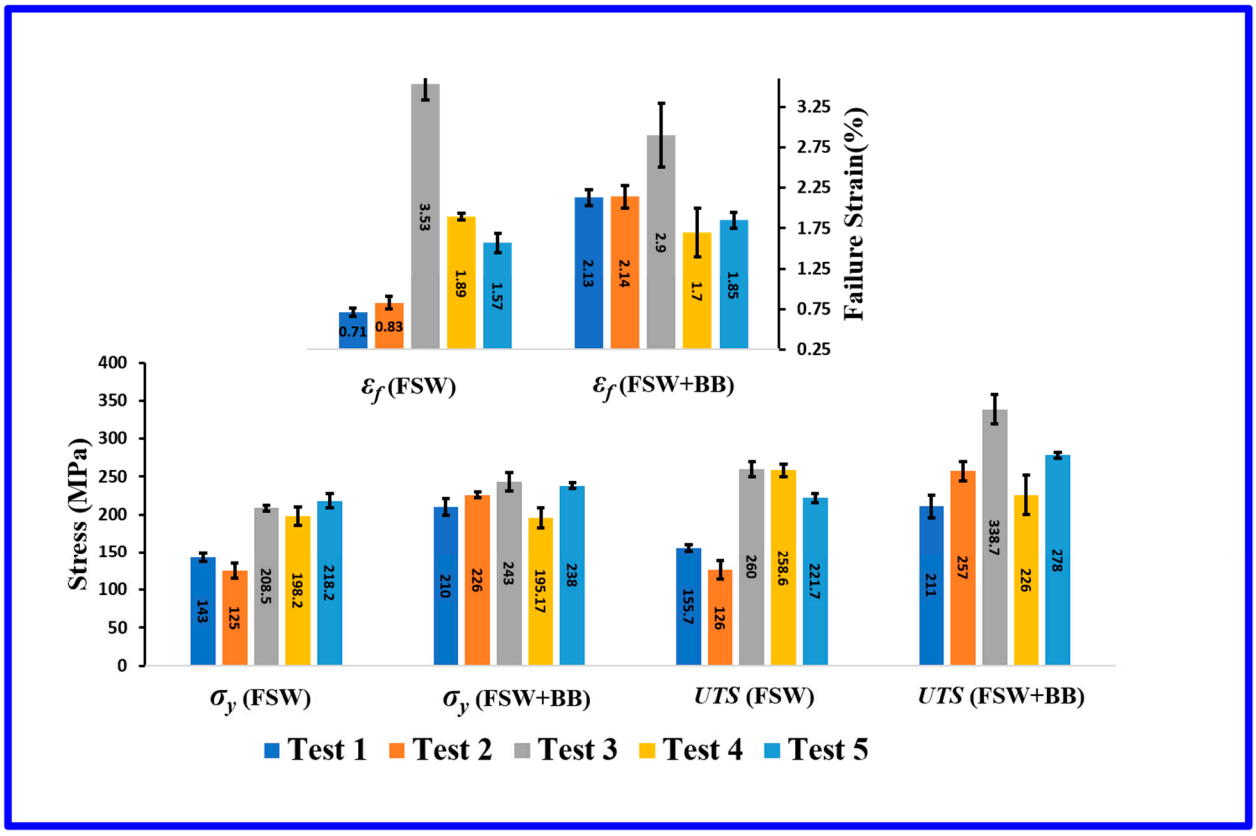

Figure 12. Comparison of mechanical characteristics (σ_y, *UTS*, ε_f) for FSW and FSW + BB specimens.

Based on the abovementioned, the burnishing operation can have favorable or detrimental effects on FSWed specimens depending on welding or burnishing parameters. In the following, the authors of this paper tried to reduce the deleterious effects of the burnishing treatment by changing the strategy. Therefore, in this experiment, two FSW tests, 3 and 4, were considered, and a double-sided BB (DBB) operation was performed on them (Figure 13a). Here, the tensile test showed that location of the failure line was closer to the centerline than FSW and FSW + BB specimens (Figure 13b). Investigations showed that running double-sided BB enhances and improves more mechanical characteristics than BB (single-sided). For Test 4, Figure 12 shows that the values of σ_y, *UTS* and ε_f of the FSW + BB specimens change by −1.5%, −12.6% and −10% compared to the FSW sample, while performing double-sided burnishing on the FSW specimens (Test 4) increases the mentioned characteristics by 13%, 6% and 5.8%, respectively (Figure 13c). On contrary, using the last strategy of burnishing in FSW Test 3 causes a change of −47.5% in failure strain, while performing BB produced a change in −17.8% of failure strain. Although the

DBB strategy seems to reduce the unfavorable effects of burnishing (single-sided), in some cases its performance is worse than single-sided burnishing operation.

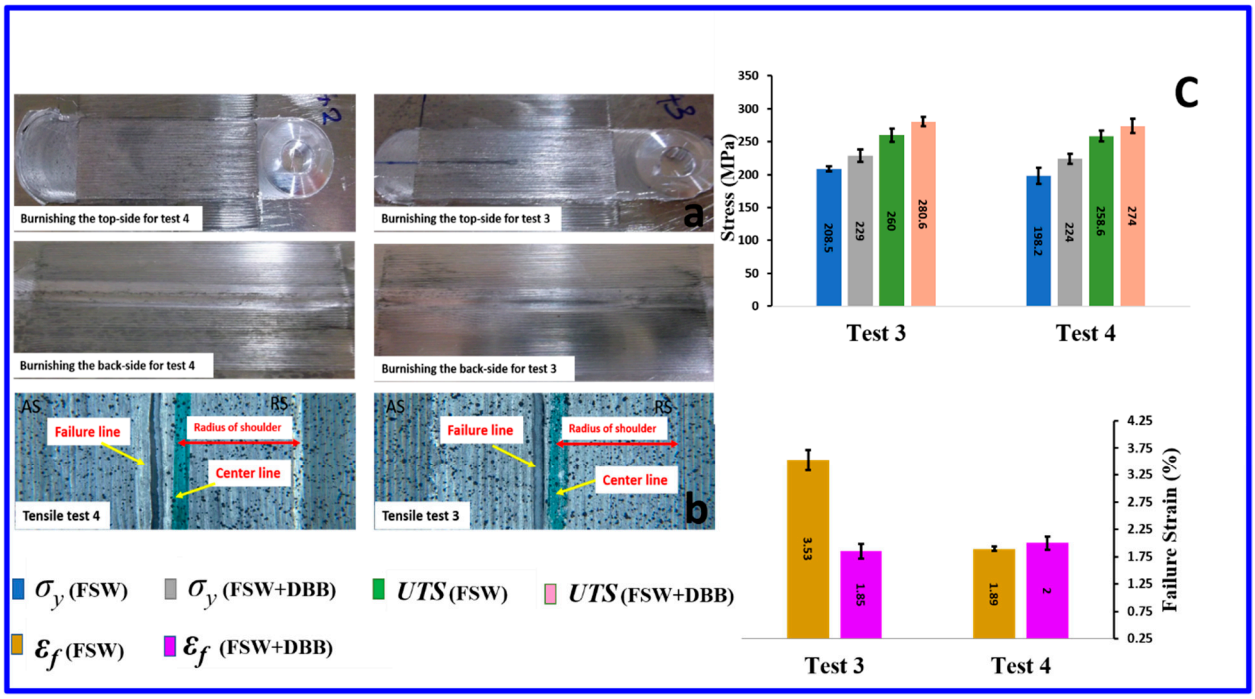

Figure 13. (**a**) Double-sided BB; (**b**) location of fracture line; (**c**) σ_y, *UTS*, ε_f for FSW tests 3 and 4 after DBB operation.

3.4. Residual Stress Evolution in an Integrated Numerical Model (in As-Welded and FSW + BB Specimens)

One of the origins of residual stresses in FSW can be as a consequence of interactions among thermal history (time and temperature) and deformation (stress and strain). The presence of residual stresses can have detrimental or beneficial effects on the service life and performance of pieces [1]. On the other hand, plastic deformation resulting from other processes (in particular, BB) causes a significant alteration of the residual stresses, inducing compressive stresses on the surface layer that enhance fatigue strength and corrosion resistance. Therefore, the challenge that arises is how the residual stress state after the application of BB on the FSWed specimen alters.

The present work shows the residual stress evolution at the surface and in-depth in FSW and in the FSW + ball burnishing process through the numerical model. These issues will be discussed further in two sub-sections. Attempts have been made to validate the residual stress in the Lagrangian model using the study of Benchman et al. [29], who performed a simulation and experimental estimation of the residual stresses on FSW of 2024-T3 aluminum alloy. The actual dimensions in the experimental test of the study were modeled (according to the procedure in Reference [15], which is demonstrated in Figure 14a) and, finally, the residual stresses resulting from the simulation are compared with the experimental residual stresses obtained in the Benchman's study, which is shown in Figure 14b. The deviation of the experimental and simulation values along the transverse path perpendicular to the welding direction is less than 6%. The greatest deviation appears at the center point of the pin. Because the pin is not considered in the simulation and only the frictional heat of the tool is taken into account in the Lagrangian model, the real value of the plastic deformation occurring in the experimental study is greatly reduced in the simulation, and values of residual stresses in this zone will be affected. Generally speaking, Figure 14b signifies the robust approach implemented in the simulation of FSW. The residual stress evolution (in terms of values and shape profile) obtained from FSW + BB simulation are compared with experimental results from Reference [11].

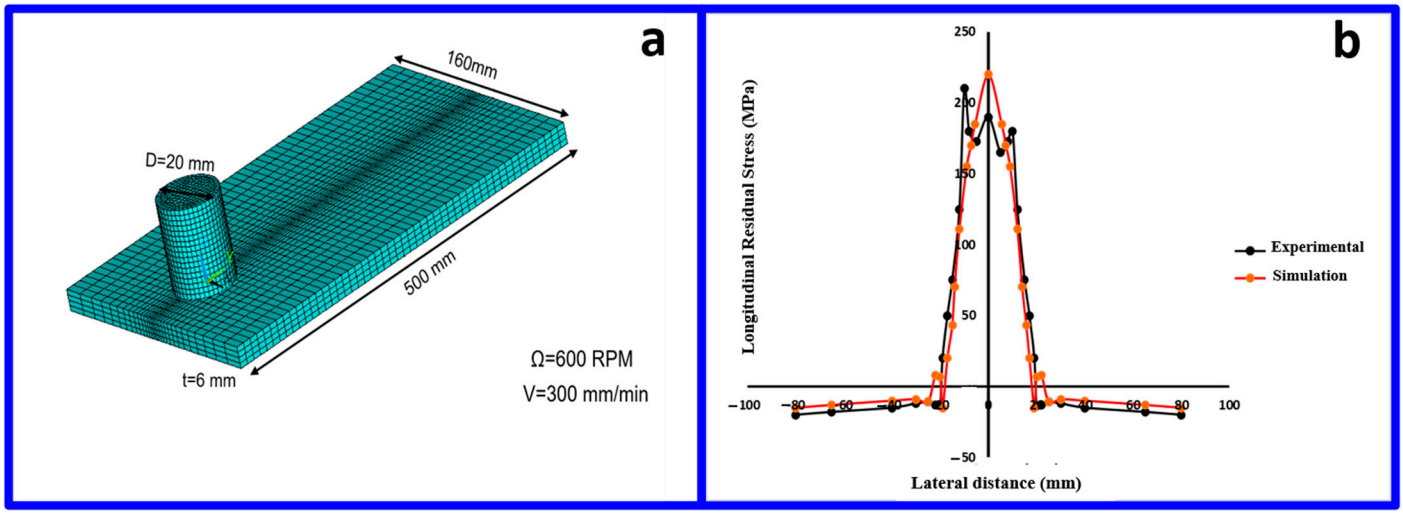

Figure 14. (**a**) FEM modeling and verification of the Lagrangian approach of [15]; (**b**) simulation of the RS of the FSW process and comparison with experimental data.

3.4.1. Residual Stresses Evolution in FSW

After the retraction of the tool, the residual stresses were obtained before and after fixture release. Since the residual stress distribution denotes a similar trend independent of FSW parameters, the residual stress contour (in common scale) in Figure 15 is limited to Test 2. Prior to the release, transverse residual stresses are greater than longitudinal residual stresses. After the release, due to the relaxation stress, the residual stresses decrease, but longitudinal residual stress (LRS) is now greater than transverse residual stress. Figure 14 signifies the NZ that has the highest values of LRS. By moving away from the centerline of the weld, a greater reduction in the values of LRS occurs. The residual stress evolution at the end of the welding to the release fixture for Test 2 is displayed in Figure 16. Figure 16 (which is limited to the NZ) suggests that the nature of the residual stresses in the welded region is mostly tensile. The magnitude of RS can be as great as the yield strength of the material. Here, however, the residual stress values are almost higher than experimental results in Ref. [1]. This is a result of the nature of the fixture system, the geometry of the plates and the neglecting of the pin in the simulation. It is worth mentioning that cutting the welded samples may lead to the relaxation of residual stress, resulting in underestimation of residual stress in the experimental results [1]. The maximum values of residual stress appear after cooling (before release fixture). A significant decrease in residual stress was observed after the release of the fixture, which is in agreement with [30]. Figure 16a shows that the value of LRS (after release) on the advancing side is almost higher than that of the retreating side. Comparing Figure 16a,b shows that LRS is the dominant stress component in the weld zone [31]. To emphasize LRS further (in particular, LRS evolution in-depth and comparison of FSW parameters and their effect on the RS), more information can be found in the next sub-section.

3.4.2. Residual Stress Evolution in BB of FSW Specimens

As mentioned above, before performing BB on FSW specimens, modification of the welding zone has to be done in accordance with the stress–strain curve obtained in the tensile test of the FSW samples. According to the result in Section 3.3, the most dominant parameter to distinguish plasticity behavior between Test 1 and Test 5 is the rotational speed of the tool. Therefore, to represent the behavior of the welding zone, the stress–strain curve of FSW in Test 2 is used for tests 2 and 1 (for both of them, ω = 550 rpm) and the stress–strain curve of FSW Test 4 is applied for tests 4 and 5 (for both of them, ω = 1100 rpm). Defining the multilinear isotropic hardening material in ANSYS® requires that the slope be positive in the multilinear data [32]. Therefore, part of the data in the curve with the positive slope was used to define the behavior of the welded zone (Figure 17).

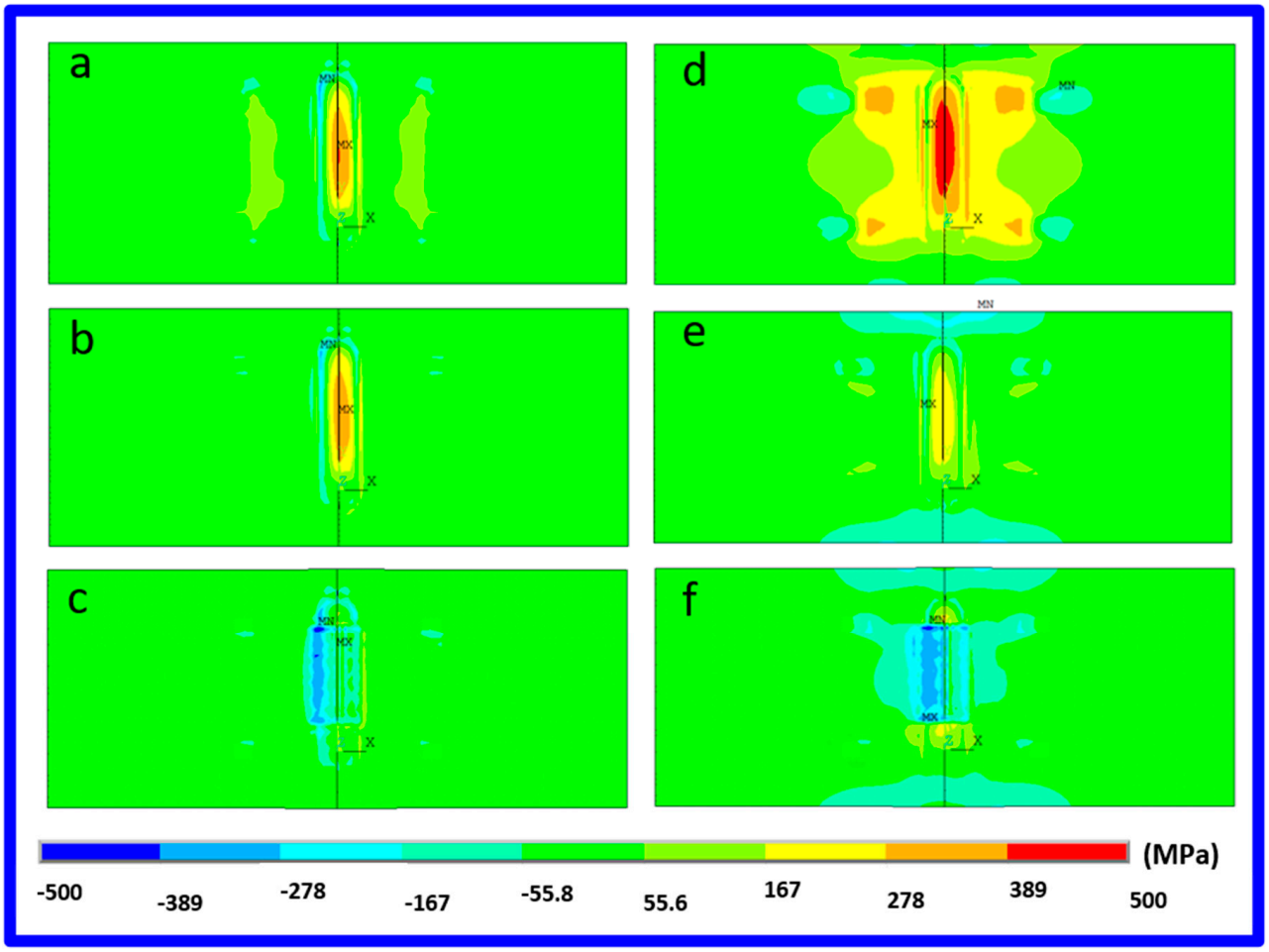

Figure 15. Evolution of stress during the FSW+ BB process for Test 2: longitudinal stress (**a**) before and (**b**) after the release of the fixture, and (**c**) after BB; transverse stress (**d**) before and (**e**) after the release of the fixture, and (**f**) after BB. (MX and MN shown in the figure are maximum and minimum values of residual stress, respectively).

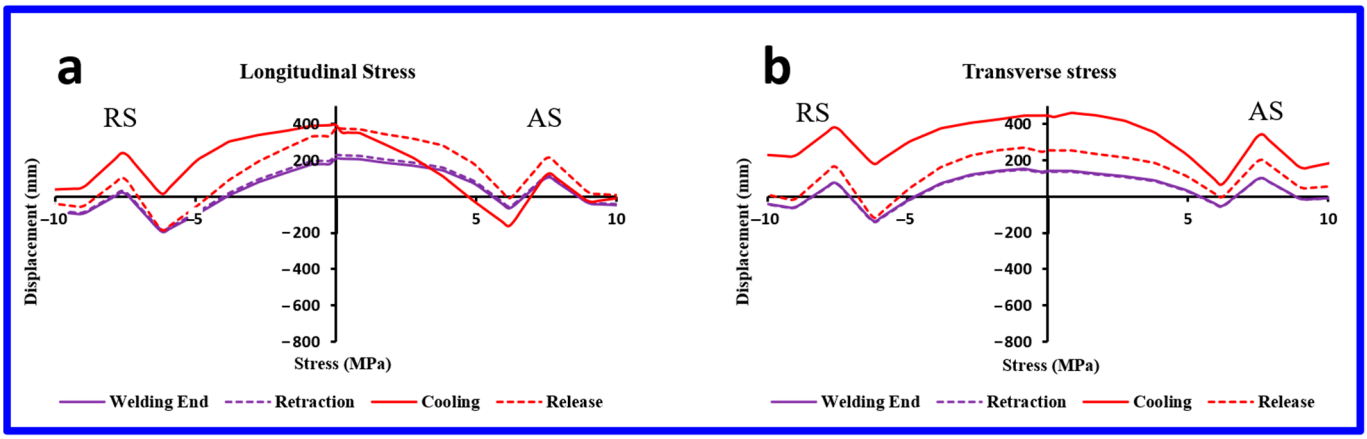

Figure 16. Variation of the stress during the FSW process for Test 2: (**a**) longitudinal and (**b**) transverse stress along the lateral path through the middle of the weld line at the surface.

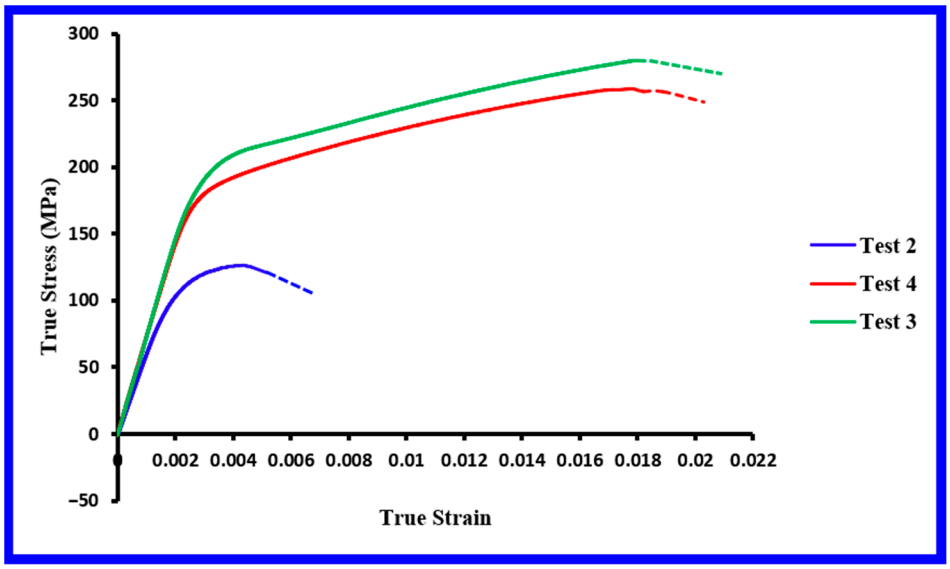

Figure 17. Stress–strain curves for modification of the material behavior in the welded zone.

The BB process is performed using the displacement control method. Figure 18 shows that, due to strain hardening, As the number of tracks increases, the vertical displacement of the pilot node (located in the center of the ball) decreases. After P_{12}, it stabilizes at approximately 42 µm (Figure 18).

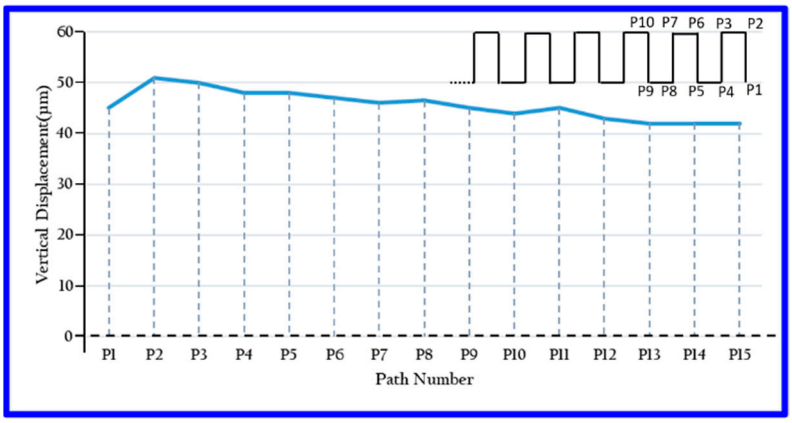

Figure 18. Display of the vertical displacement of the pilot node vs. the number of paths (P_i-P_{i+1} is a part of the zigzag path traveled by the ball).

To avoid providing redundant material and because the LRS is considered in the model validation in Figure 14, further discussion in this section focuses on changes in the LRS on the vicinity of the tool ($-10.5 \leq x \leq 10.5$ mm). Figure 19a shows the LRS contour due to FSW on the surface and along the thickness for half of the model (the cutting line a-a (Figure 5) passes through the middle of the weld line). The highest LRS (after welding) was witnessed in the proximity of the weld line. Figure 19b,c show the longitudinal residual stress changes after welding and after BB of the welded specimen along the transverse path passing through the middle of the weld line. The lower the welding speed (comparison of Test 1 and Test 2 or Test 4 with Test 5), the lower the value of LRS and its gradient in the wider region [29,31]. The highest value of LRS, which is about 402 MPa, was observed for Test 5 (after welding). The LRS distribution presents similar trends, independent of the FSW and BB parameters. However, it is expected that the experimental values are much lower than the predicted values [1]. Figure 19c shows that increasing the rotational speed of the tool induces more tensile residual stresses, which is different from the results mentioned in Ref. [1]. In Ref. [1], when the rotational speed of the tool varies from 254 to 653 rpm, the

tensile residual stress decreases with the increasing tool rotational speed. Here, it seems that this trend changes with the further increase of rotational speed (more than 550 rpm) and a higher tensile RS appears, which is in agreement with [33]. Figure 19b,c show that tensile residual stress after welding in the AS region is higher than in the RS region, which is in conformity with the results of References [1,33].

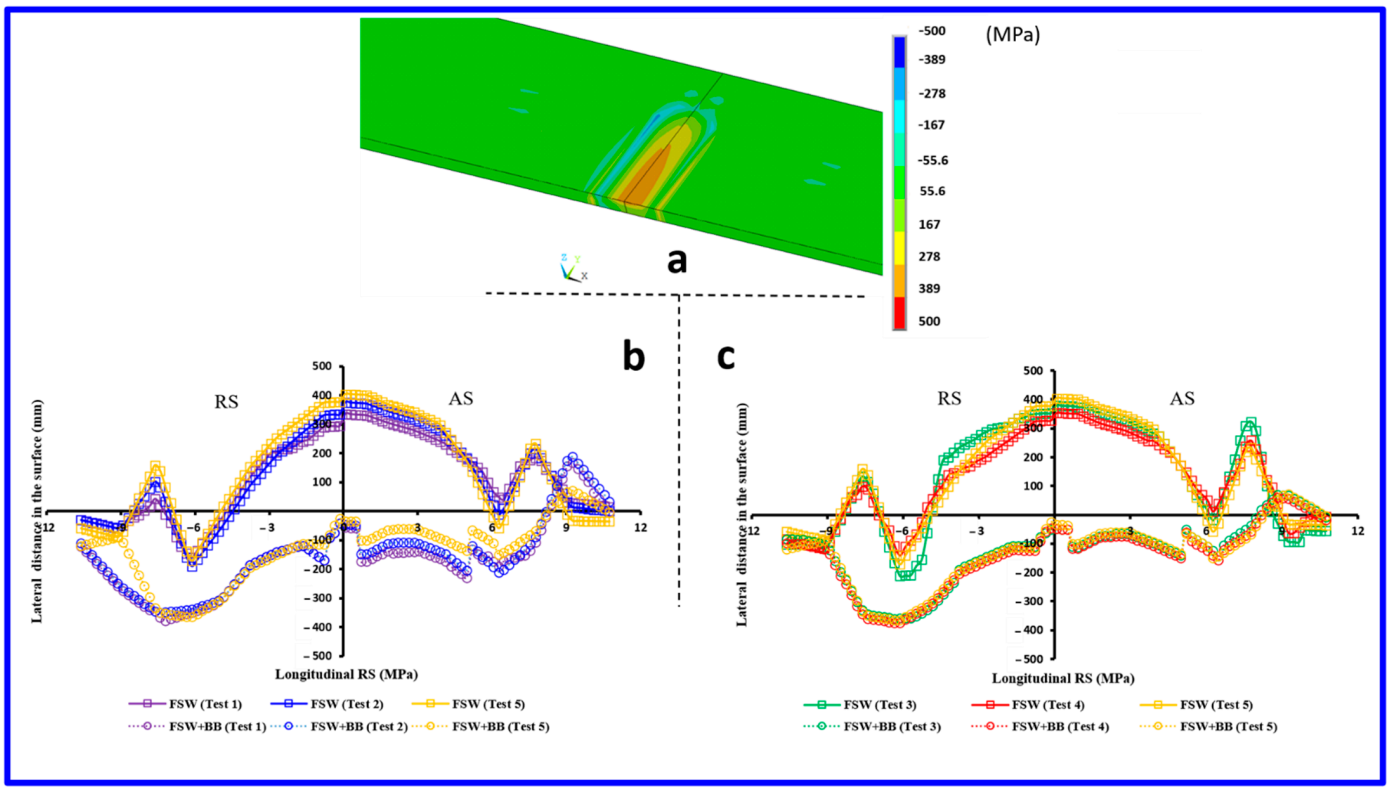

Figure 19. (**a**) LRS contour for Test 2 after FSW process. LRS changes along the transverse path at the surface in the middle of the weld line, after FSW and BB for (**b**) tests 1,2 and 5; (**c**) tests 3, 4 and 5.

After applying the BB process on the as-welded samples, the LRS on the surface decreased and the surface was in compression (Figure 19b,c). This process induces the most negative stress in the RS region of FSW specimens. Although the residual stress can be increased by raising the burnishing force or the number of passes, Test 1 (Figure 19b) and Test 4 (Figure 19c) possess the greatest compressive residual stresses, which are −220, −150 MPa in the AS region and −377, −364 MPa in RS region, respectively. This value (−377 MPa) is 16% less than the value reported in Reference [11]. It looks as if the as-weld samples produced with lower welding speed possess the greatest compressive LRS at the surface after performing BB.

Figure 20 exhibits the evolution of in-depth LRS after FSW and the subsequent BB process. The simulations show that the distribution of residual stress is partly dependent on the defined path along the thickness. Therefore, in each test, two different paths are specified, the starting points of which are where the residual stress profile of FSW has a relative maximum (see Figure 19b,c): a path along the thickness and passing through the AS region (X = 0.85 mm), and a path along the thickness and passing through the RS region at the border of the shoulder. It is worth mentioning that the shape of the in-depth residual stress profile is affected by the mesh. Since the finite element model used in welding has been subsequently applied in the simulation of the burnishing process, the time of analysis and its implementation with the available facilities causes the number of elements used along the thickness to be limited. As shown in Figure 20, the distribution of in-depth residual stresses after welding can be ascending or descending, depending on the path.

The in-depth LRS distribution along the path defined in the RS region is ascending and possess a lower gradient compared to the other path (a path defined in AS).

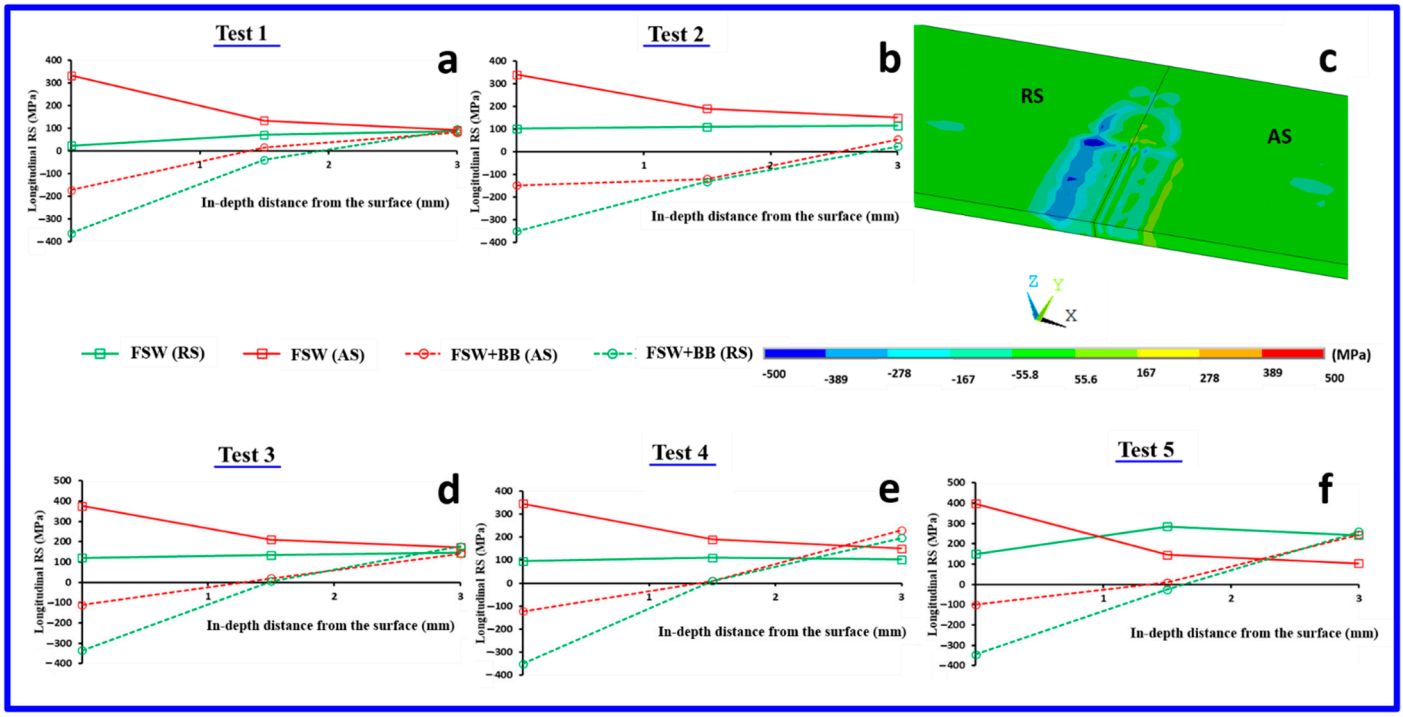

Figure 20. (**a**,**b**,**d**–**f**) Comparison in-depth residual stress distribution after FSW and BB (**c**) LRS contour for test two after FSW + BB.

However, after BB, an ascending trend in the in-depth LRS distribution is predicted, which is in harmony with [11]. By performing BB on FSW specimens, welding residual stress values along the depth up to 50% of the total plate thickness are decreased and converted to compressive stresses (Figure 20). However, the depth of effect obtained from the simulation is slightly greater than that in Ref. [11]. When the BB process is deployed on the weld specimen, the in-depth residual stresses along the paths defined in the RS and AS regions start from −365 to −345 MPa and −172 to −100 MPa, respectively. Higher values of LRS (after BB) are found beyond the middle of the depth and these are tensile stresses. Moving further along the depth, in-depth LRS (after BB) may exceed the corresponding values of the FSW process (Figure 20d–f). The results shown in Figure 20b lack the deleterious effect of the burnishing process. The simulations of Figure 20 signify that after the BB process is performed on the welded specimens created at high rotational speeds, the values of in-depth LRS in these specimens will be most increased near the bottom of the plate (for Test 5, LRS reached +260 MPa).

4. Conclusions

In this paper, the combination of two processes—FSW and BB—on aluminum alloy of 2024-T3 was investigated experimentally and simulated. By performing the BB treatment under constant conditions in experiments designed for FSW, the substantial findings of this research, which are extractive, can be summarized as follows.

Increasing the rotational speed of the tool and the welding speed have opposite effects on the superficial roughness. The first improves the surface (11% to 36%) and the latter worsens it. On the other hand, the effect of BB on surface quality improvement is more pronounced in welding specimens created using low rotational speeds.

In this study, when BB treatment is deployed on the welded samples, hardness experiences an increase of about 22%.

Compared to the original material, FSW treatment has detrimental effects on mechanical characteristics and decreases them. On the other hand, the BB process enhanced the mechanical properties in some tests after welding. However, this process worsened some characteristics in some tests.

In the tensile test, all welded specimens fractured in the AS zone near the pin (between the pin radius and the shoulder radius), which is approximately the boundary of the transition from TMAZ to HAZ (with the lowest value of hardness).

The presentation of the integrated numerical model FSW + BB (without direct experimental measurement of residual stresses for validation) partially reveals the evolution of residual stresses from tensile to compressive stresses at the surface and along the thickness, due to the BB process on FSWed samples.

Deeper than the middle of the plate, residual stresses due to the BB process may be greater than welding residual stresses. In fact, there is a detrimental effect of BB on the back of the FSWed samples. This may be eliminated or lessened using the DBB strategy.

Along with the application of the BB process to reinforce strength, corrosion and fatigue resistance of a welding area that has suffered a thermal softening (in aviation industry, in particular), investigating the effect of other, new BB methods, such as vibration-assisted BB on FSW specimens, or modifying the simulation using image processing techniques (which deliver point-to-point welding properties in the welding area) can be challenges for future research.

Author Contributions: Conceptualization, S.H., M.D.Z., J.A.T.-R. and R.J.-M.; Methodology, R.J.-M., C.A. and J.A.T.-R.; Software, C.A. and H.M.; Validation, C.A., J.A.T.-R., J.L.-F. and R.J.-M.; Formal Analysis, C.A., J.A.T.-R. and R.J.-M.; Investigation, R.J.-M., J.A.T.-R. and C.A.; Resources, J.A.T.-R. and R.J.-M.; Data Curation, C.A., M.D.Z. and J.L.-F.; Writing—Original Draft Preparation, C.A.; Writing—Review and Editing, J.A.T.-R. and R.J.-M.; Visualization, C.A., H.M. and M.D.Z.; Supervision, S.H., J.L.-F., J.A.T.-R. and R.J.-M.; Project Administration, J.A.T.-R.; Funding Acquisition, J.A.T.-R. and R.J.-M. All authors have read and agreed to the published version of the manuscript.

Funding: Financial support for this study was provided by the Iran Ministry of Science, Research and Technology (Grant no.: S/24/88), which is greatly appreciated.

Informed Consent Statement: Not applicable.

Data Availability Statement: The raw/processed data required to reproduce these findings cannot be shared at this time, as the data also forms part of an ongoing study.

Conflicts of Interest: The authors declare no conflict of interest.

References

1. Kumar, N.; Mishra, R.S.; Baumann, J.A. *Residual Stresses in Friction Stir Welding*, 1st ed.; Butterworth-Heinemann: Waltham, MA, USA, 2013. [CrossRef]
2. Lohwasser, D.; Chen, Z. (Eds.) *Friction Stir Welding: From Basics to Applications*, 1st ed.; Elsevier: North Andover, MA, USA, 2009. [CrossRef]
3. Moreira, P.M.; De Figureueiredo, M.A.; De Castro, P.M. Fatigue behavior of FSW and MIG weldments for two aluminum alloys. *Theor. Appl. Fract. Mech.* **2007**, *48*, 169–177. [CrossRef]
4. Jenarthanan, M.P.; Varma, C.V.; Manohar, V.K. Impact of friction stir welding (FSW) process parameters on tensile strength during dissimilar welds of AA2014 and AA6061. *Mater. Today Proc.* **2018**, *5*, 14384–14391. [CrossRef]
5. Hassan, A.M. The effects of ball-and roller-burnishing on the surface roughness and hardness of some non-ferrous metals. *J. Mater. Process. Technol.* **1997**, *72*, 385–391. [CrossRef]
6. El-Axir, M.H. An investigation into roller burnishing. *Int. J. Mach. Tools Manuf.* **2000**, *40*, 1603–1617. [CrossRef]
7. Nalla, R.K.; Altenberger, I.; Noster, U.; Liu, G.Y.; Scholtes, B.; Ritchie, R.O. On the influence of mechanical surface treatments—Deep rolling and laser shock peening—On the fatigue behavior of Ti-6Al-4V at ambient and elevated temperatures. *Mater. Sci. Eng. A.* **2003**, *355*, 216–230. [CrossRef]
8. García-Granada, A.A.; Gomez-Gras, G.; Jerez-Mesa, R.; Travieso-Rodriguez, J.A.; Reyes, G. Ball-burnishing effect on deep residual stress on AISI 1038 and AA2017-T4. *Mater. Manuf. Process.* **2017**, *32*, 1279–1289. [CrossRef]
9. Jerez-Mesa, R.; Travieso-Rodriguez, J.A.; Landon, Y.; Dessein, G.; Lluma-Fuentes, J.; Wagner, V. Comprehensive analysis of surface integrity modification of ball-end milled Ti-6Al-4V surfaces through vibration-assisted ball burnishing. *J. Mater. Process. Technol.* **2019**, *267*, 230–240. [CrossRef]

10. Prevéy, P.S.; Shepard, M.J.; Smith, P.R. The effect of Low Plasticity Burnishing (LPB) on the HCF performance and FOD resistance of Ti-6AI-4V. In Proceedings of the 6th National Turbine Engine High Cycle Fatigue (HCF) Conference, Jacksonville, FL, USA, 5–8 March 2001. Available online: https://apps.dtic.mil/sti/pdfs/ADA447005.pdf (accessed on 20 July 2015).
11. Prevéy, P.; Mahoney, M.W. Improved fatigue performance of friction stir welds with low plasticity burnishing: Residual stress design and fatigue performance assessment. In Proceedings of the THERMEC'2003 International Conference on Processing & Manufacturing of Advanced Materials, Madrid, Spain, 7–11 July 2003; Volume 426, pp. 2933–2940. Available online: https://www.lambdatechs.com/wp-content/uploads/239.pdf (accessed on 20 July 2015).
12. Başak, H.; Özkan, S.; Taşkesen, A. Application of burnishing process on friction stir welding and investigation of the effect of burnishing process on the surface roughness. *Exp. Tech.* **2011**, *35*, 8–16. [CrossRef]
13. Huang, Y.X.; Wan, L.; Lv, S.X.; Zhang, Z.; Liu, H.J. New technique of in situ rolling friction stir welding. *Sci. Technol. Weld. Join.* **2012**, *17*, 636–642. [CrossRef]
14. Rodríguez, A.; Calleja, A.; López de Lacalle, L.N.; Pereira, O.; González, H.; Urbikain, G.; Laye, J. Burnishing of FSW aluminum Al-Cu-Li components. *Metals* **2019**, *9*, 260. [CrossRef]
15. Amini, C.; Hasanifard, S.; Zehsaz, M.; Jerez-Mesa, R.; Travieso-Rodriguez, J.A. Friction stir welding of AA2024-T3: Development of numerical simulation considering thermal history and heat generation. *Int. J. Adv. Manuf. Technol.* **2021**, *117*, 2481–2500. [CrossRef]
16. Jerez-Mesa, R.; Travieso-Rodriguez, J.A.; Gomez-Gras, G.; Lluma-Fuentes, J. Ultrasonic Vibration-Assisted Ball Burnishing Tool. Referencia de patente P201730385, 21 March 2017.
17. Sayahi, M.; Sghaier, S.; Belhadjsalah, H. Finite element analysis of ball burnishing process: Comparisons between numerical results and experiments. *Int. J. Adv. Manuf. Technol.* **2013**, *67*, 1665–1673. [CrossRef]
18. Korzynski, M. A model of smoothing slide ball-burnishing and an analysis of the parameter interaction. *J. Mater. Process. Technol.* **2009**, *209*, 625–633. [CrossRef]
19. Bouzid Saï, W.; Saï, K. Finite element modeling of burnishing of AISI 1042 steel. *Int. J. Adv. Manuf. Technol.* **2005**, *25*, 460–465. [CrossRef]
20. Skalski, K.; Morawski, A.; Przybylski, W. Analysis of contact elastic-plastic strains during the process of burnishing. *Int. J. Mech. Sci.* **1995**, *37*, 461–472. [CrossRef]
21. Hua, Y.; Liu, Z.; Wang, B.; Jiang, J. Residual stress regenerated on low plasticity burnished Inconel 718 surface after initial turning process. *J. Manuf. Sci. Eng.* **2019**, *141*, 121004. [CrossRef]
22. Amini, C.; Jerez-Mesa, R.; Travieso-Rodriguez Llumà, J.; Estevez-Urra, A. Finite element analysis of ball burnishing on ball-end milled surfaces considering their original topology and residual stress. *Metals* **2020**, *10*, 638. [CrossRef]
23. Bhushan, R.K.; Sharma, D. Investigation of mechanical properties and surface roughness of friction stir welded AA6061-T651. *Int. J. Mech. Mater. Eng.* **2020**, *15*, 7. [CrossRef]
24. Meng, X.; Huang, Y.; Cao, J.; Shen, J.; dos Santos, J.F. Recent progress on control strategies for inherent issues in friction stir welding. *Prog. Mater. Sci.* **2021**, *115*, 100706. [CrossRef]
25. Zhu, R.; Gong, W.B.; Cui, H. Temperature evolution, microstructure, and properties of friction stir welded ultra-thick 6082 aluminum alloy joints. *Int. J. Adv. Manuf. Technol.* **2020**, *108*, 331–343. [CrossRef]
26. Xie, Y.; Meng, X.; Huang, Y. Entire-process simulation of friction stir welding—Part 1: Experiments and simulation. *Welding J.* **2022**, *101*, 5. [CrossRef]
27. Gachi, S.; Aissani, M.; Baudin, T.; Helbert, A.; Brisset, F.; Gautrot, S.; Mathon, M.H.; Bradai, D.; Boubenider, F. The microstructure, texture and mechanical properties of friction stir welded aluminum alloy. *Russ. J. Non-Ferrous Met.* **2020**, *61*, 523–533. [CrossRef]
28. Nouri, A.; Kazemi Nasrabadi, M. Ductile Failure Prediction of Friction Stir Welded AA7075-T6 Aluminum Alloy Weakened by a V-notch. *J. Stress. Anal.* **2019**, *4*, 113–124. [CrossRef]
29. Bachmann, M.; Carstensen, J.; Bergmann, L.; dos Santos, J.F.; Wu, C.S.; Rethmeier, M. Numerical simulation of thermally induced residual stresses in friction stir welding of aluminum alloy 2024-T3 at different welding speeds. *Int. J. Adv. Manuf. Technol.* **2017**, *91*, 1443–1452. [CrossRef]
30. Zhu, X.K.; Chao, Y.J. Numerical simulation of transient temperature and residual stresses in friction stir welding of 304L stainless steel. *J. Mater. Process. Technol.* **2004**, *146*, 263–272. [CrossRef]
31. Riahi, M.; Nazari, H. Analysis of transient temperature and residual thermal stresses in friction stir welding of aluminum alloy 6061-T6 via numerical simulation. *Int. J. Adv. Manuf. Technol.* **2011**, *55*, 143–152. [CrossRef]
32. ANSYS, Inc. *ANSYS Mechanical APDL Theory Reference*; Release 17.0 (Version 17); ANSYS Inc.: Canonsburg, PA, USA, 2016.
33. He, J.; Ling, Z.; Li, H. Effect of tool rotational speed on residual stress, microstructure, and tensile properties of friction stir welded 6061-T6 aluminum alloy thick plate. *Int. J. Adv. Manuf. Technol.* **2016**, *84*, 1953–1961. [CrossRef]